Supplementary Information

Ferroelectric Memristors Optimized in Thickness for Short-Term Memory-Driven Reservoir Computing

Junhyeok Park[1], and Sungjun Kim[1]*

Afflications:

[1]Division of Electronics and Electrical Engineering, Dongguk University, Seoul 04620, South Korea

*** Corresponding author:**

Sungjun Kim (Email: sungjun@dongguk.edu)

Supplementary figures

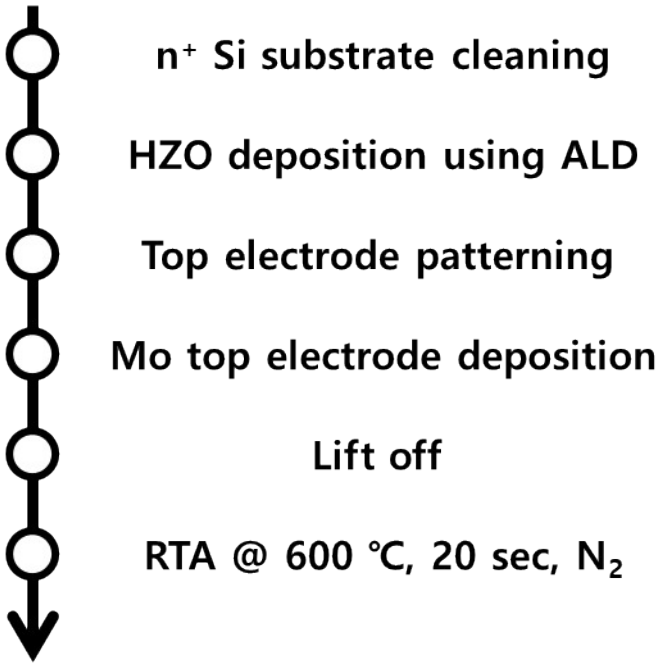

Figure S1. Fabrication process of the Mo/HZO/n^+ Si device.

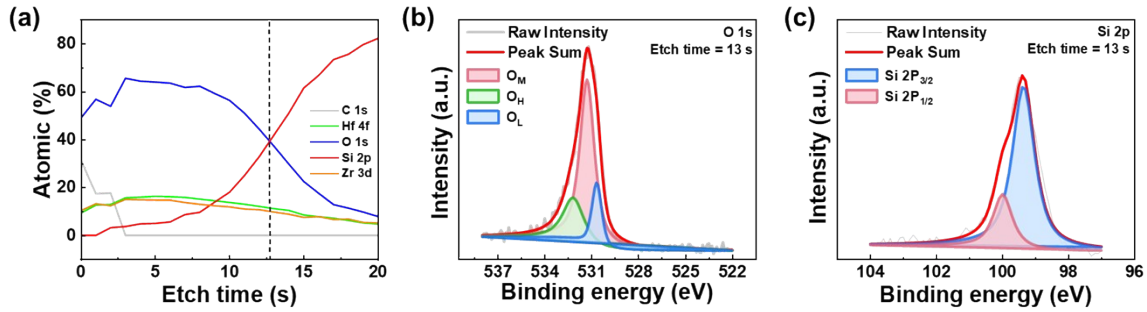

Figure S2. (a) Elemental composition as a function of etching time. (b) XPS peak spectra representing (b) O 1s and (c) Si 2p of the SiO2 layer.

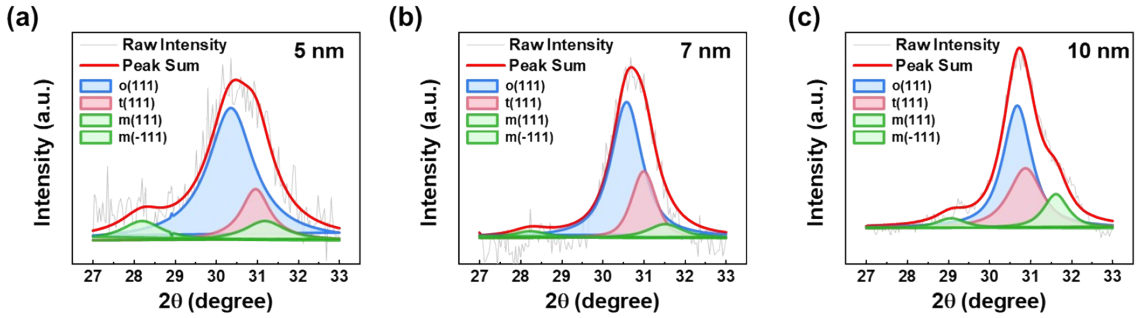

Figure S3. Deconvoluted GIXRD spectra of the devices with HZO film thickness of (a) 5 nm, (b) 7 nm, (c) 10 nm.

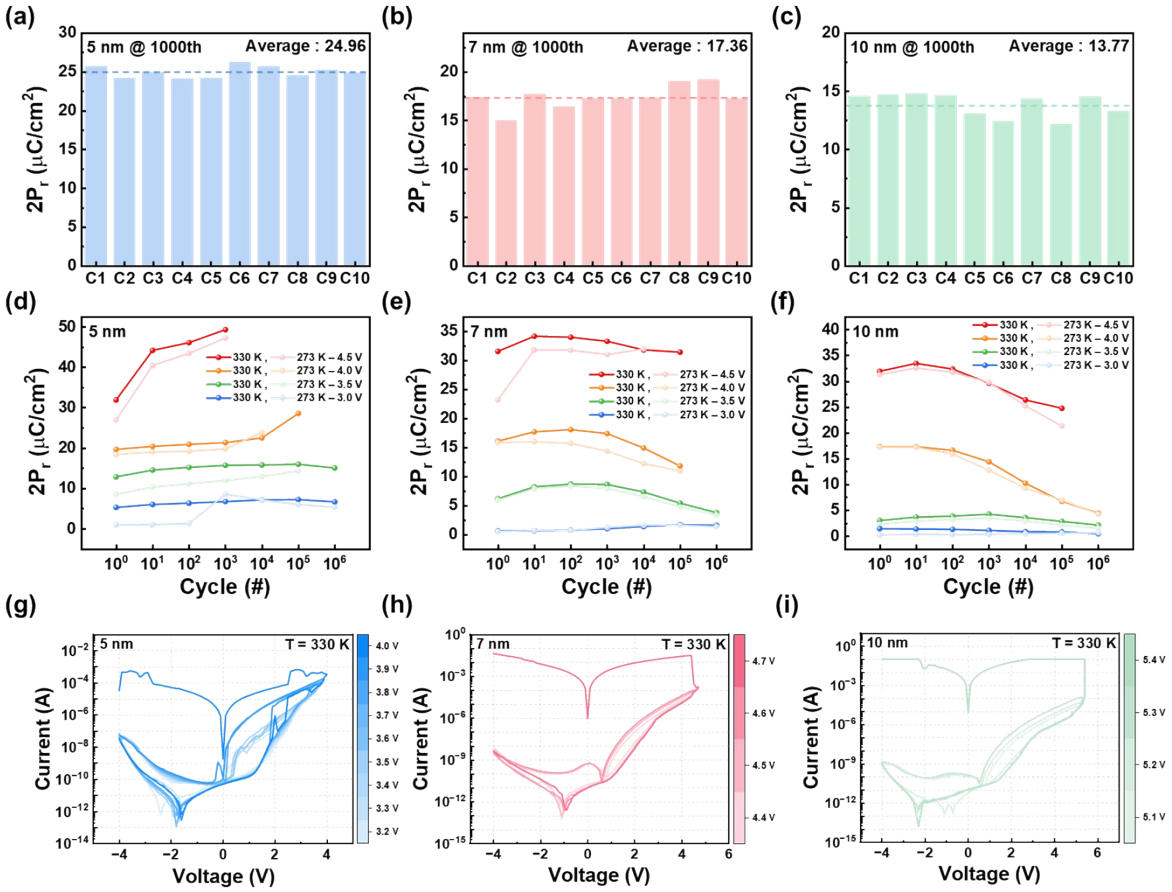

Figure S4. Cell-to-cell variation of 2Pr values for devices with HZO thicknesses of (a) 5 nm, (b) 7 nm, and (c) 10 nm. Endurance characteristics measured at 273 K and 330 K for HZO thicknesses of (d) 5 nm, (e) 7 nm, and (f) 10 nm. Current–voltage (I–V) characteristics measured at 330 K for HZO thicknesses of (g) 5 nm, (h) 7 nm, and (i) 10 nm.

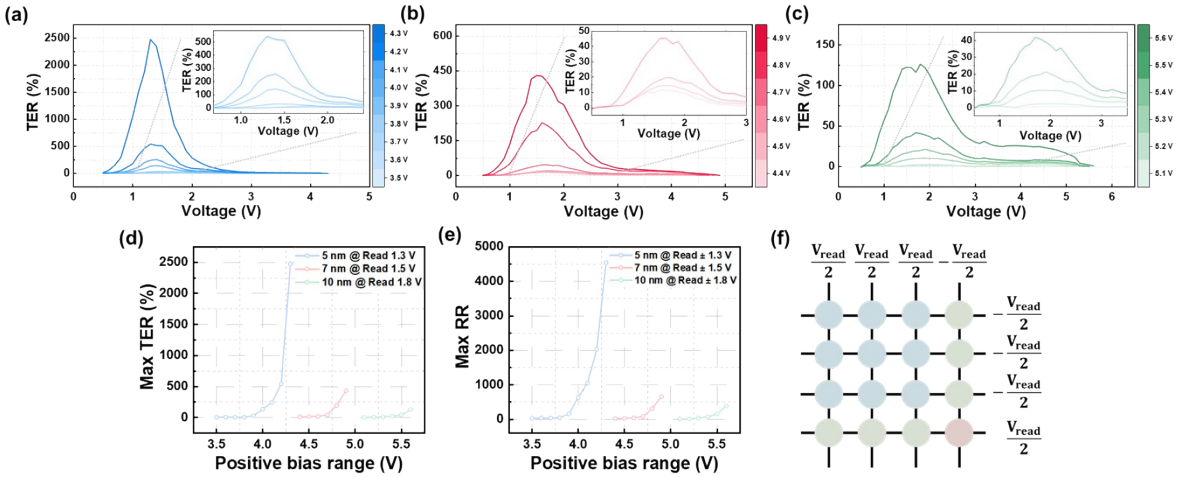

Figure S5. Maximum TER as a function of voltage for devices with HZO thicknesses of (a) 5 nm, (b) 7 nm, and (c) 10 nm. Bias-dependent values of (d) Max TER and (e) Max RR for each device. (f) The modified half-bias scheme.

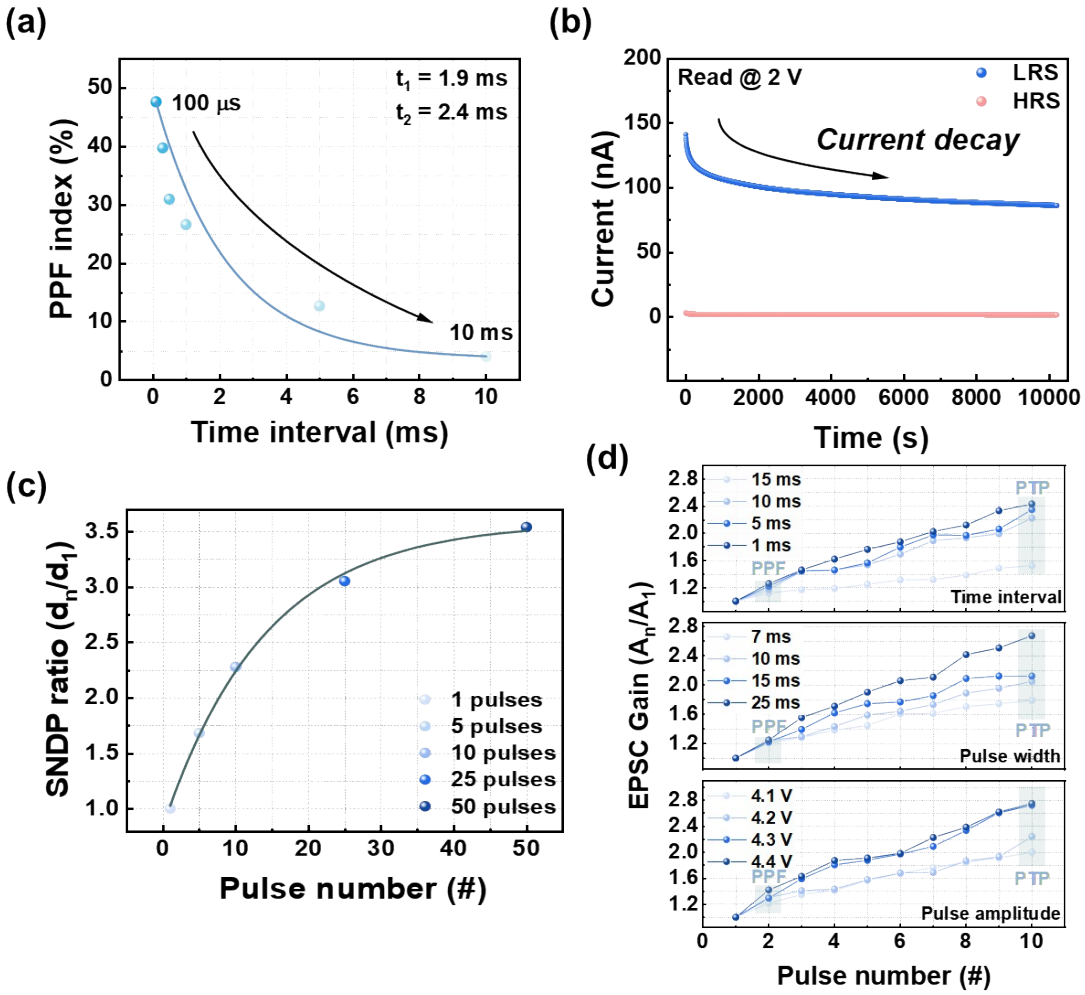

Figure S6. (a) PPF index as a function of spike interval between two pulses and the time decay constants. (b) Retention characteristics at a read voltage of 2 V over 10,000 s. (c) SNDP ratio. (d) SRDP, SDDP, SADP gain.

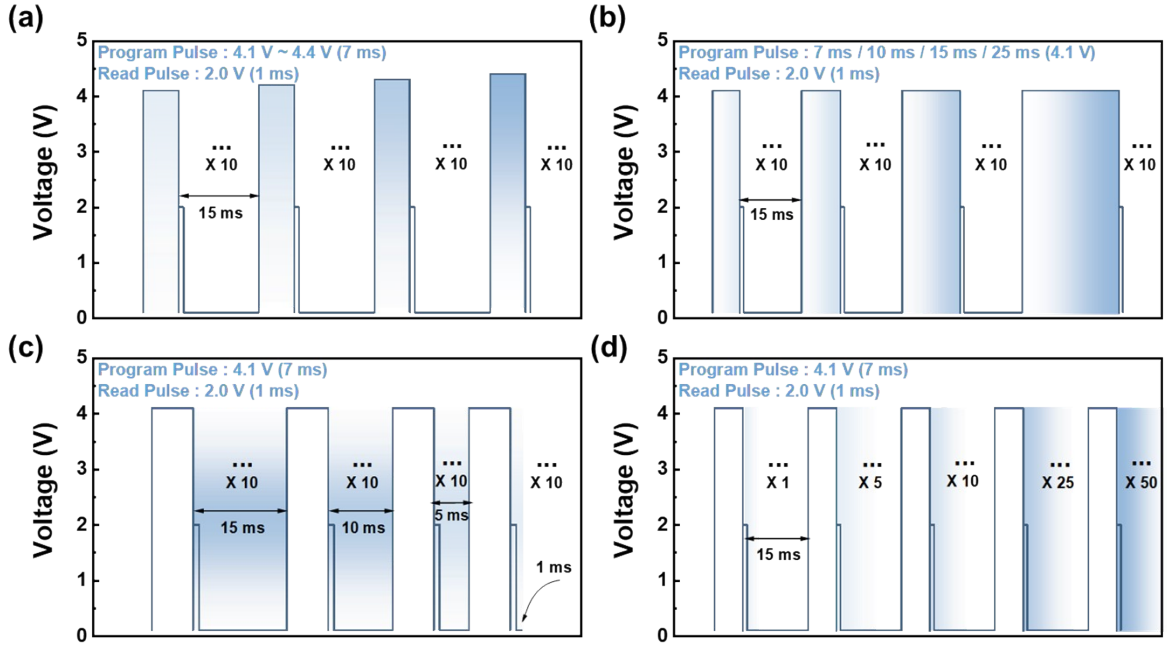

Figure S7. Pulse schemes used to verify the characteristics of (a) SADP, (b) SWDP, (c) SRDP, and (d) SNDP.

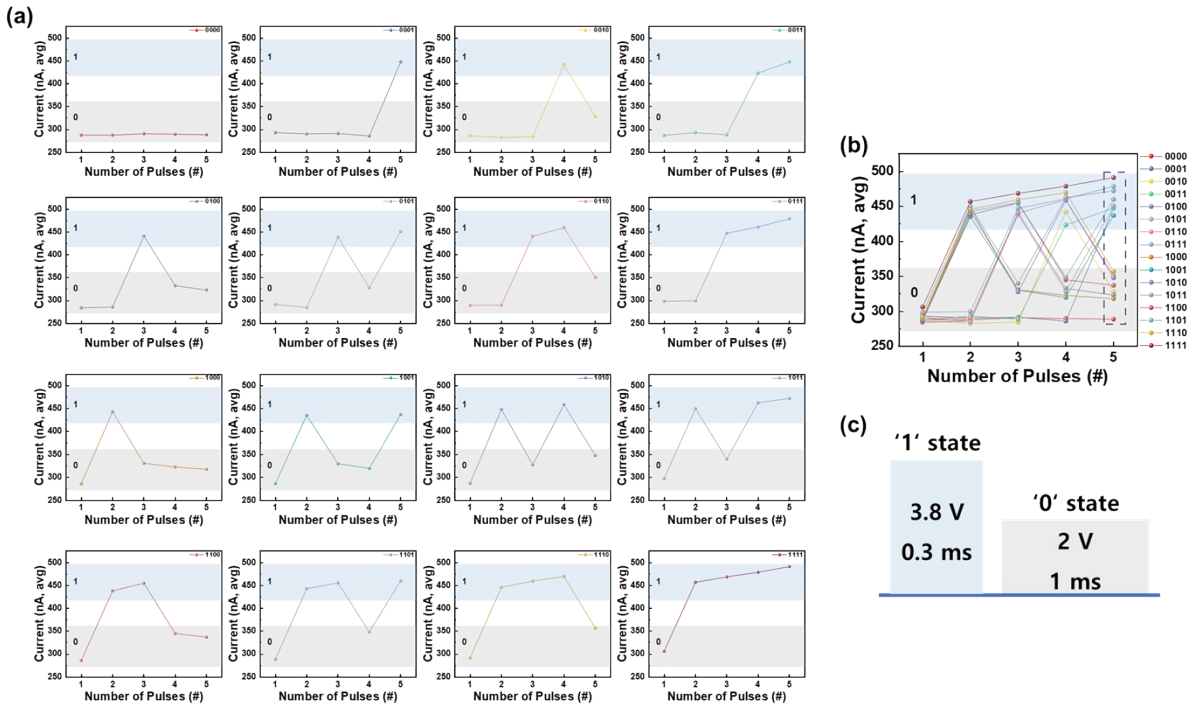

Figure S8. (a) 16 different four-bit states, each measured from a single cell. (b) Pulse schemes for the ′1′ and ′0′ states. (c) Average current levels of 16 four-bit states in the short-term memory device, obtained by averaging over five cells.

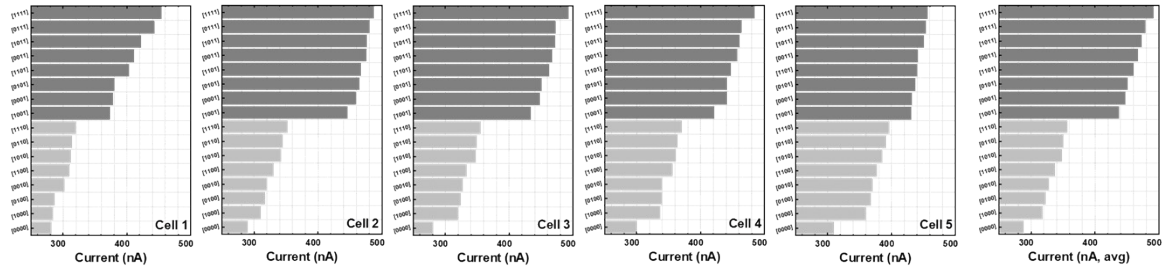

Figure S9. Separation characteristics of reservoir states obtained from each cell and averaging.

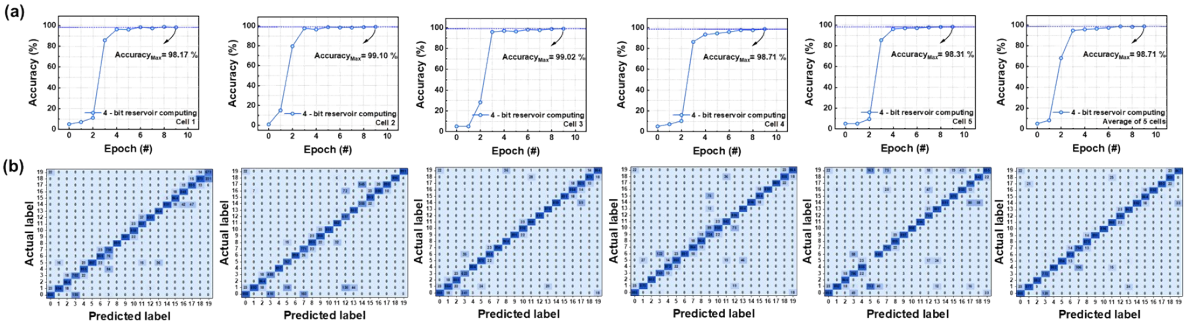

Figure S10. (a) Pattern recognition accuracy of the Hand MNIST device, measured for each cell. (b) Confusion matrix of Hand MNIST recognition using a 4-bit model with diagonal weights, measured for each cell.

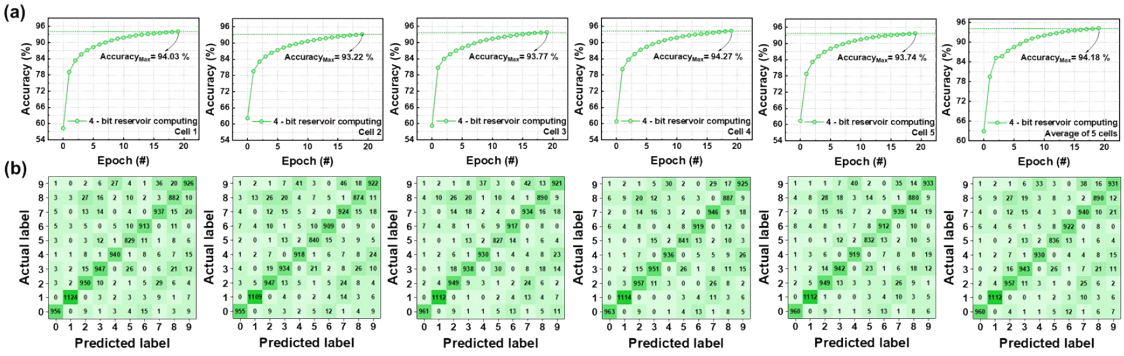

Figure S11. (a) Pattern recognition accuracy of the MNIST device, measured for each cell. (b) Confusion matrix of MNIST digit recognition using a 4-bit model with diagonal weights, measured for each cell.

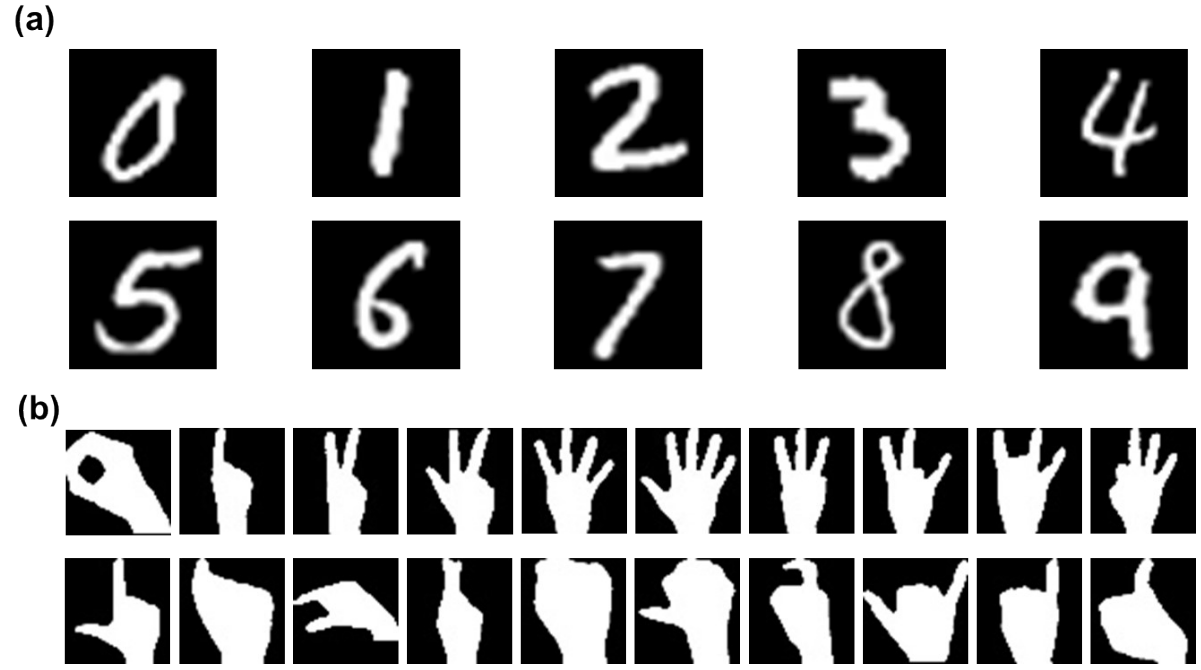

Figure S12. Sample images from (a) MNIST, (b) Hand MNIST datasets.